Supplementary Information for

Realizing Mildly Acidic Proton Battery via Surface Functionalization

*Jianyong Zhang[1], Kai Fu[1], Kai Du[4], Cheng Wen[1], Jingyuan Yu[1], Chunhua Han[1], Yuxiang Hu[4], and Lin Xu[1,2,3]**

1 State Key Laboratory of Advanced Technology for Materials Synthesis and Processing, School of Materials Science and Engineering, Wuhan University of Technology, Wuhan 430070, China.

2 Hubei Longzhong Laboratory, Wuhan University of Technology (Xiangyang Demonstration Zone), Xiangyang 441000, Hubei, China.

3 Hainan Institute, Wuhan University of Technology, Sanya 572000, China.

4 Key Laboratory of Advanced Functional Materials of Education Ministry of China, College of Materials Science and Engineering, Beijing University of Technology, Beijing, 100124, China.

Address:122 Luoshi Road, Wuhan 430070, Hubei, China

E-mail: linxu@whut.edu.cn

Experimental section

Material preparation

To obtain MoO_3 nanowires, 2 g $(NH_4)_6Mo_7O_{24}•4H_2O$ was dissolved in 90 ml deionized water. Then 10 ml nitric acid (70%) was slowly dropped into the solution and stirred for 10 min. The mixture was subsequently transferred to a 100 mL Teflon-lined autoclave and then heated at 180 ^oC for 24 h. The white precipitation was washed with deionized water at least five times and dried in an oven at 80 ^oC for 10 h. The MoO_3 nanowires powder was obtained.

CuFe-TBA was obtained by the precipitation method. $CuSO_4$ solution (0.2 M) was slowly dropped into $K_3Fe(CN)_6$ (0.2 M) with a mass ratio of 1:1. The precipitation was washed at least three times via centrifuge with DI water, and then the components were dried in an oven 80 °C for 24 h. Finally, the powder of CuFe-TBA was obtained.

Material Characterizations

The in-situ X-ray diffraction (XRD) patterns were probed on a monochromator Cu source Kα X-ray (λ = 1.5406 Å) by a D8 Discover X-ray diffractometer. GASA software was used to perform XRD refinement. SEM and EDS mapping were taken via a JEOL JSM-7100F in 20 kV (voltage). TEM images were collected with a JEM-2100F and a Thermo Fischer Titan G2 60-300 microscope. X-ray photoelectron spectroscopy (XPS) was introduced to evaluate the valence of elements (Type: VG MultiLab 2000). FT-IR was conducted on a Thermo Nicolet Nexus instrument. ESR measurement was collected with a JESFA200 instrument. The Raman spectra were probed with 532 nm

laser resources by Horiba LabRAM HR Evolution. The PT-2S plasma cleaner is utilized with a continuously variable power source operating at a frequency of 50 kHz and an RF power of 300 W. The electrode is treated with 2-14 min shown in Figure S3a. In this plasma treatment, the carbon groups that are grafted at the surface of the electrode are derived from organic compounds such as binders (PVDF).

The measurement of zeta potential allows for the assessment of the electrical properties at the solid-liquid interface, specifically the ζ potential of particles within a dispersed system. This measurement serves as a means to evaluate and determine the positive and negative characteristics of surface charges exhibited by the material. The charge properties of the material surface can be derived by measuring the Zeta potential of the particles. The electrode powder of MoO_3 was subjected to oxygen plasma treatment with a mass of 0.1 g. Subsequently, the plasma-treated powder was dispersed in an aqueous solution (0.01 M H_2SO_4). The solution was then analyzed using a Zeta potential analyzer to determine the surface charge characteristics of the electrode material. Zeta potential is collected with Zetasizer Advance.

The in situ XRD was tested via the Bruker Discover X-ray diffractometer on a monochromator Cu source Kα X-ray (λ = 1.5406 Å). The schematic illustration of the in-situ XRD cell is demonstrated in Figure S21. The cell of in-situ XRD is tested as a symmetric cell. The MoO_3 was used as a working electrode and the MoO_3 was used as a counter electrode and reference electrode. The cell was tested with 0.01 M H_2SO_4 at 1A g^{-1}. The shell of the in-situ XRD cell was made of Ti metal. The testing window of

electrodes in cells sealed with a polyimide sheet with a thickness of 50 μm. The scan rate of Bruker Discover X-ray diffractometer was 10 s per degree.

Electrochemical characterization

Preparations of MO (MoO_3) and OPMO (oxygen plasma treatment MoO_3) electrode: MO electrode was prepared by mixing active material (MoO_3) with conductive additive (acetylene black) and binder (polytetrafluoroethylene, PVDF or PTFE) in a mass ratio of 7: 2: 1 in NMP solvent to form a slurry. Then, the slurry was quickly filmed on Ti foil. Then it was dried at 90 ^oC in the oven for 2 h. The obtained electrode was cut into small disks with a diameter of 12 mm. Additionally, these disks were prepared as MO electrodes. OPMO electrode was prepared after oxygen plasma treatment (plasma cleaner PT-2S in Figure S1). Firstly, the OPMO electrode adhered to the chamber of plasma cleaner PT-2S. Then, the oxygen flow is introduced into the chamber for 30 min to exclude the air. Later, the oxygen was ionized in the plasma cleaner for 8 min. The OPMO electrode was obtained.

One that should be mentioned is that OPMO electrodes should not be reserved for a too long time in the air in case of redox by slight reduction/oxidization components. In-situ X-ray diffraction (XRD) analysis was conducted with electrolyte of 0.01 M H_2SO_4.

For the TBA electrode, the procedure was the same, the TBA electrode was prepared by mixing active material (TBA) with a conductive additive (acetylene black) and binder (polytetrafluoroethylene, PVDF) in a mass ratio of 7: 2: 1. Then the mixture was mixed with NMP solvent to form slurry and slurry quickly filmed on Ti foil. Otherwise,

carbon cloth substrates were also processed the same way for additional cycling. Then it was dried at 90 ^{o}C in the oven for 2 h. The obtained electrode was cut into small disks with a diameter of 12 mm.

The electrochemical quartz crystal microbalance (EQCM) tests were conducted on the quartz crystal microbalance at 25 ^{o}C. The OPMO electrode is spread on a crystal that is coated gold as the working electrode, Pt is the counter electrode and $Hg/HgSO_4$ is the reference electrode. The CV curve was tested with CHI400C.

The Swagelok cell was used to enable close distance for the current collector and its assembling is shown in Figure S2. The traditional electrode in the three-electrode cell has a long distance for the electrode which increases the polarization of the electrode and augments the uncertainty of the electrochemical test for the battery. Both symmetric electrodes and full batteries were tested with a coin cell. In the three-electrode cell, the electrode material is the working electrode and CDD carbon cloth is the counter electrode. A mercurous sulfate electrode is a reference electrode (MSE). In the coin cell, MoO_3 is the anode and TBA is the cathode and the mass ratio for the anode and cathode for the full battery is 1:1. For the in-situ XRD test, MoO_3 works as a symmetric electrode. The area mass of electrode materials that loaded on the current collector was approximately 2.1-3.5 mg cm^{-2}. Electrochemical properties were tested with LAND CT3001A and Biologic VMP. The discharge states (1~6) in the EIS result corresponds to 0, -0.2, -0.4, -0.6, -0.8, -1 V.

Calculation formula

QCM calculation

The mass change is calculated as follows:

$\triangle f = -2fo^2 \triangle M \cdot [A \cdot sqrt(mr)]^{-1}$

Where fo is the basic resonant frequency of the crystal, A is the area of the gold plate plated on the crystal, r is the density of the crystal (2.684 $g \cdot cm^{-3}$), and m is the crystal shear coefficient ($2.947x10^{11}$ $g \cdot cm^{-1} \cdot s^{-2}$). For our crystal, these parameters are as follows: fo=7.995 MHz, A=0.196 cm^2. The f is the frequency, and M is the mass change of the electrode. The frequency change per Hertz is equivalent to 1.34 ng.

Capacitance calculations.

The energy density was calculated by the following:

$$E = \frac{C \times V}{M}$$

E presents the energy density (Wh kg^{-1}). C is the discharge capacity of the cell (mAh). V is the average discharge voltage of the cell (V). M is the total mass (Kg) of MoO_3 and consumed TBA, respectively.

To illustrate the slope of the Nyquist plot when the slope is 45° at low frequency, the relationship for Z`` and Z` in the Nyquist plot is provided in formulas (1) and (2).

$$Z` = R_\Omega + R_{ct} + \sigma\omega^{\frac{-1}{2}} \quad (1)$$

$$Z`` = \sigma\omega^{\frac{-1}{2}} + 2\sigma^2 C_d \quad (2)$$

After combining the two formulas, we get the following relationship:

$$Z`` = Z` - R_\Omega - R_{ct} + 2\sigma^2 C_d \quad (3)$$

Where Z`` and Z` are the y and x values of the Nyquist plot, R_Ω and R_{ct} are the total intercepts of the x-axis and the semicircle in the Nyquist plot. The f is the frequency that is applied in EIS (ω=2πf). C_d (capacitance) is a constant. In the Bode plot (formula

1), σ is the slope of the line (Figure S17e). When the frequency is in the low zone, the Z`` and Z` portions are simplified. The relationship between the Z`` and Z` parts is achieved by calculating from formula (3), which is a straight-line equation with a slope of 1. This straight line on the Nyquist plot has an angle of 45° (*Electrochimica Acta, 281, 2018, 170e188*), (*Solid State Ionics, 368, 2021, 115680*).

The above discussion is based on the results obtained under the ideal condition of linear diffusion of the plate electrode. While the real testing system cannot fully meet these conditions, it is often found that the slope in the Nyquist plot is not 45 degrees. There are many reasons for this phenomenon, and there are two main reasons:

(a) The electrode surface is rough without an ideal plate, so the diffusion process is partially equivalent to spherical diffusion. The angle of the line is less than 45 degrees.

(b) The inductive reactance during the measurement process will influence the slope of the angle.

In a real testing situation, the slope of the Nyquist plot at low frequency is complex. The Bode plot (formula 1) and the ion diffusion formula (4) are used to estimate the diffusion rate of the electrode in the EIS plot.

$$Z` = R_{\Omega} + R_{ct} + \sigma\omega^{\frac{-1}{2}} \quad (1)$$

$$D_{(H)^+} = \frac{R^2T^2}{2A^2n^4F^4C^2\sigma^2} \quad (4)$$

The value of R represents the gas constant (8.314 J K^{-1} mol^{-1}). T is the absolute temperature (298 K), A stands for the surface area of the electrode or current collector (1.13 cm^2), n is the number of electrons involved in the reaction (n = 1), F is the Faraday constant (96485.3383), C is the concentration of the proton ion (C is 1.68 mol cm^{-3} in this work).

In the Bode plot, σ is the slope of the Bode plot (formula 1). When applying the slop (σ) to formula (4), the diffusion rate at the electrode interface is obtained. As we can

see, the low value of slop (σ) in the Bode plot means a high diffusion rate (formula 4). The OPMO shows a lower slop value than MO (Figure S17e, 17f) indicating that the OPMO delivers a high diffusion rate.

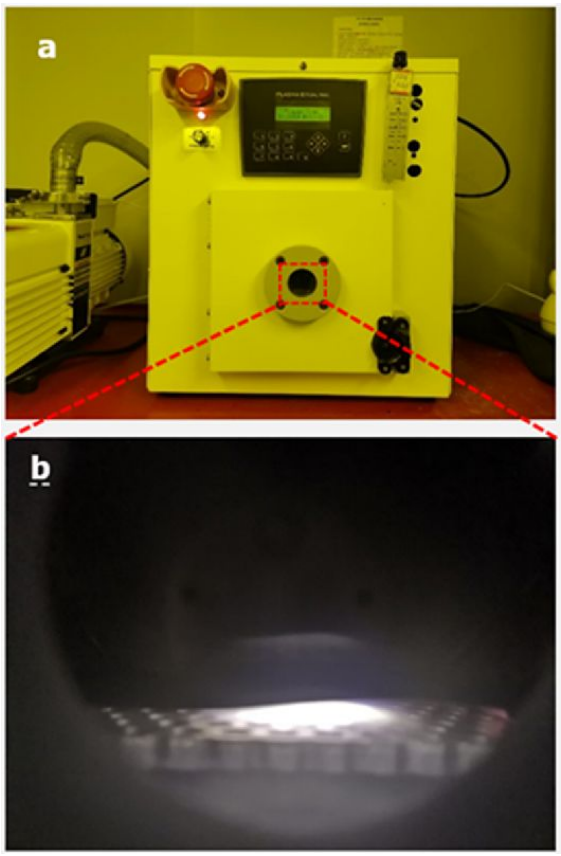

Figure S1. (a) Digital photo of O_2 plasma machine (PCD-MG). (b) The digital photo of the O_2 plasma treatment on the surface of the electrode film.

Figure S2. The digital photo of Swagelok cell.

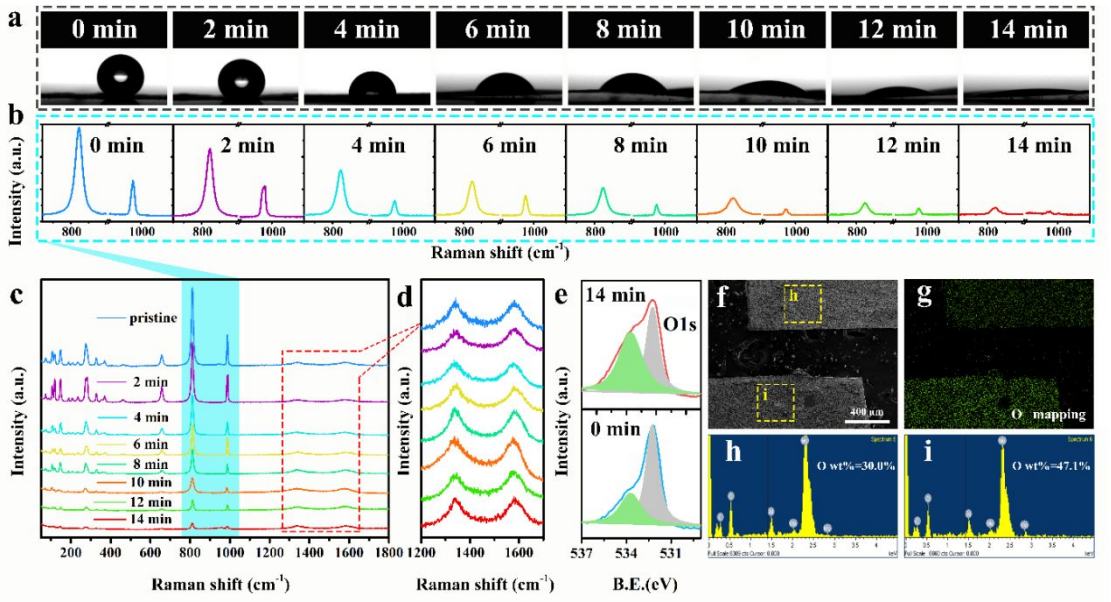

Figure S3. (a) Water contact angle photo of the electrode at different treatment periods from 0-14 min. (b) Magnified Raman spectra of MoO_3 electrode at different treatment periods from 0-14 min. (c) Full Raman spectra of the MoO_3 electrode at different treatment periods from 0-14 min. (d) Magnified D and G bands for MoO_3 electrodes at different treating periods from 0-14 min. (e) XPS spectra of the pristine electrode (0

min) and oxygen plasma-treated electrode (14 min). (f) SEM image of the pristine electrode and oxygen plasma-treated electrode. (g) Mapping of the pristine electrode and oxygen plasma-treated electrode. (h) EDS results of the pristine electrode. (i) EDS results of oxygen plasma treated electrode.

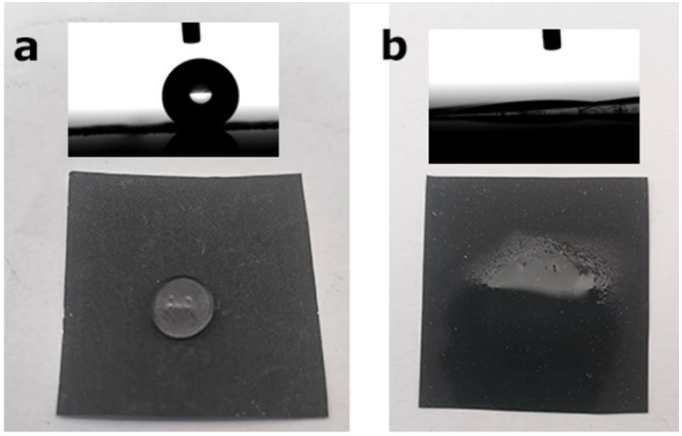

Figure S4. (a) Hydrophobic illustration of MO in 0.01 M H_2SO_4, (b) Hydrophilic illustration of OPMO in 0.01 M H_2SO_4.

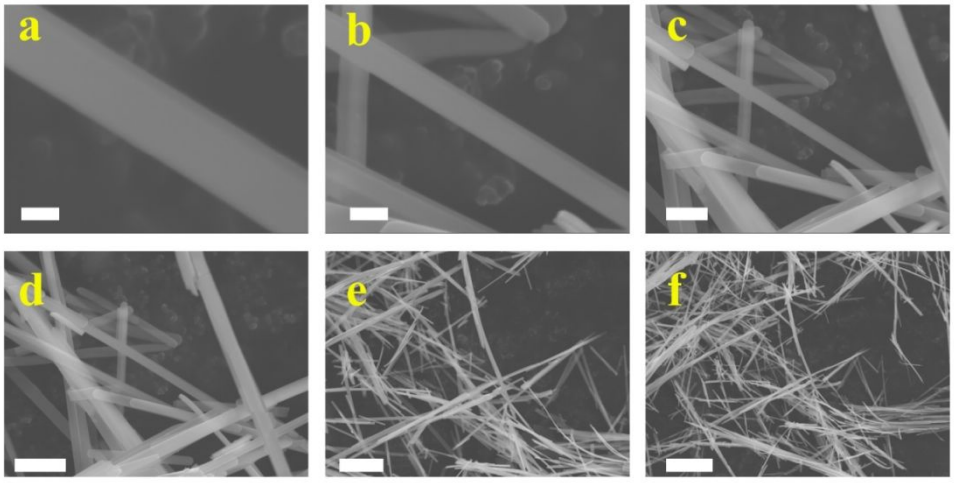

Figure S5. Scanning electron microscope (SEM) images of MoO_3 nanowires with scale bars which are corresponding to (a) 100 nm, (b) 200 nm, (c) 500 nm, (d) 1 μm, (e) 3 μm, and (f) 5 μm.

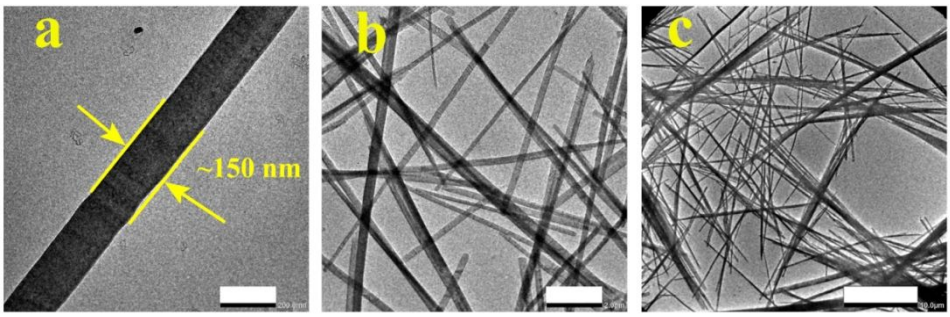

Figure S6. Transmission electron microscope (TEM) images with different scale bars (a) 200 nm, (b) 2 μm, (c) 10 μm).

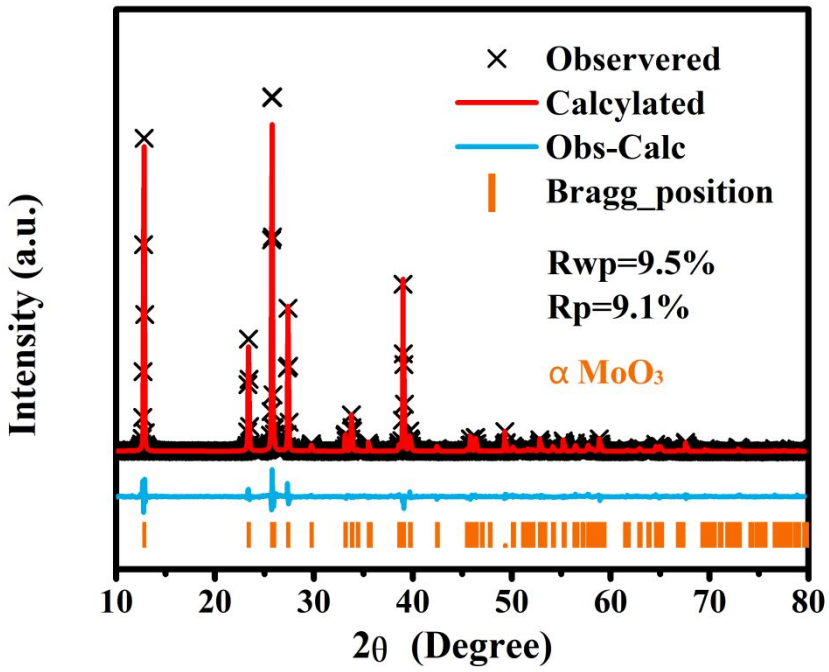

Figure S7. Rietveld refinement XRD pattern for MoO_3 nanowires.

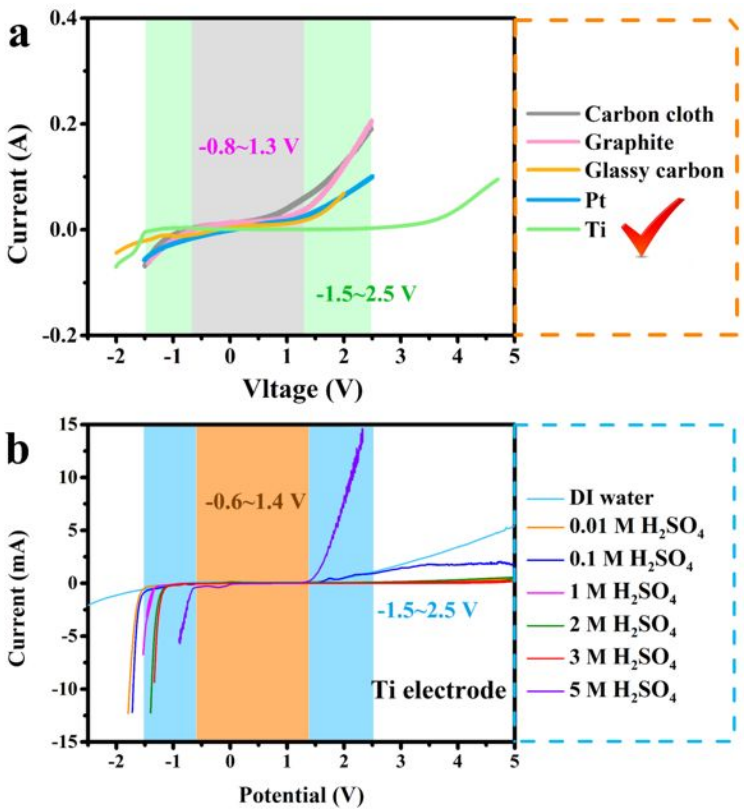

Figure S8. (a) LSV tests with different current collectors. (b) LSV tests with different concentrations of sulfuric acids in Ti current collectors.

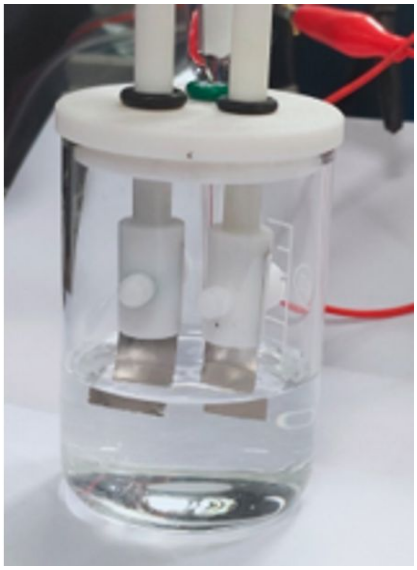

Figure S9. LSV test images of current collectors in three-electrode cells.

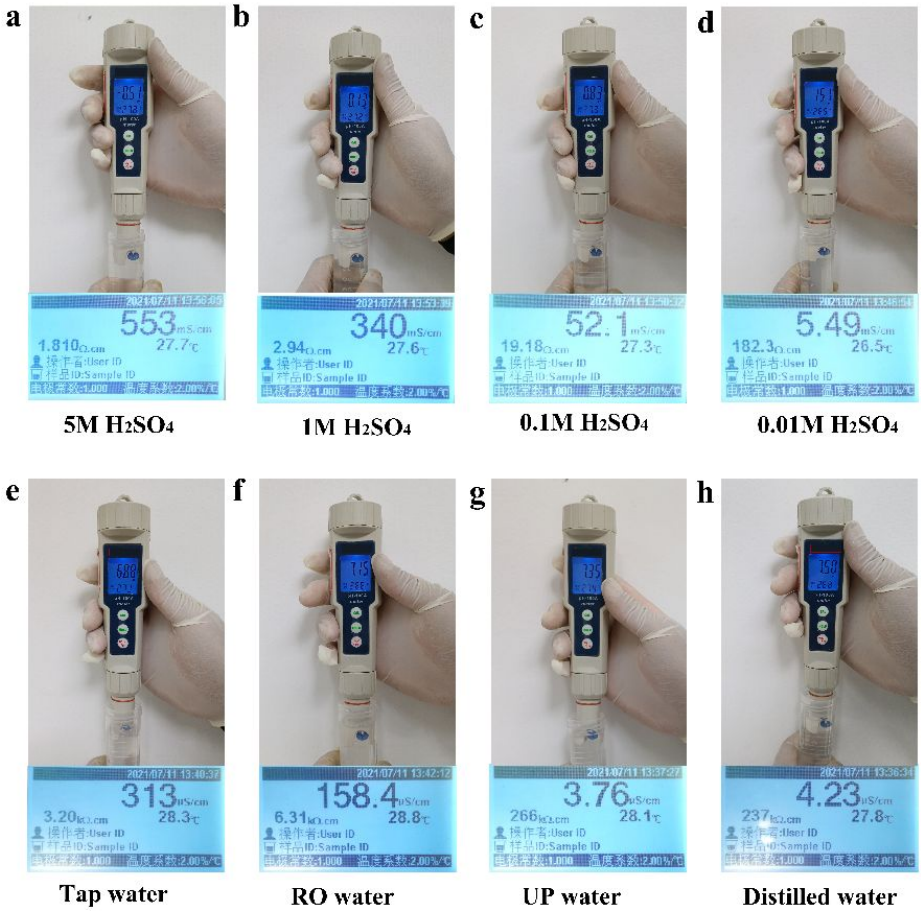

Figure S10. The pH values and conductivities of (a) 5 M H_2SO_4, (b) 1 M H_2SO_4, (c) 0.1 M H_2SO_4, (d) 0.01 M H_2SO_4, (e) tape water, (f) RO water (Reverse osmosis), (g) UP water (Ultrapure water), and (h) distilled water.

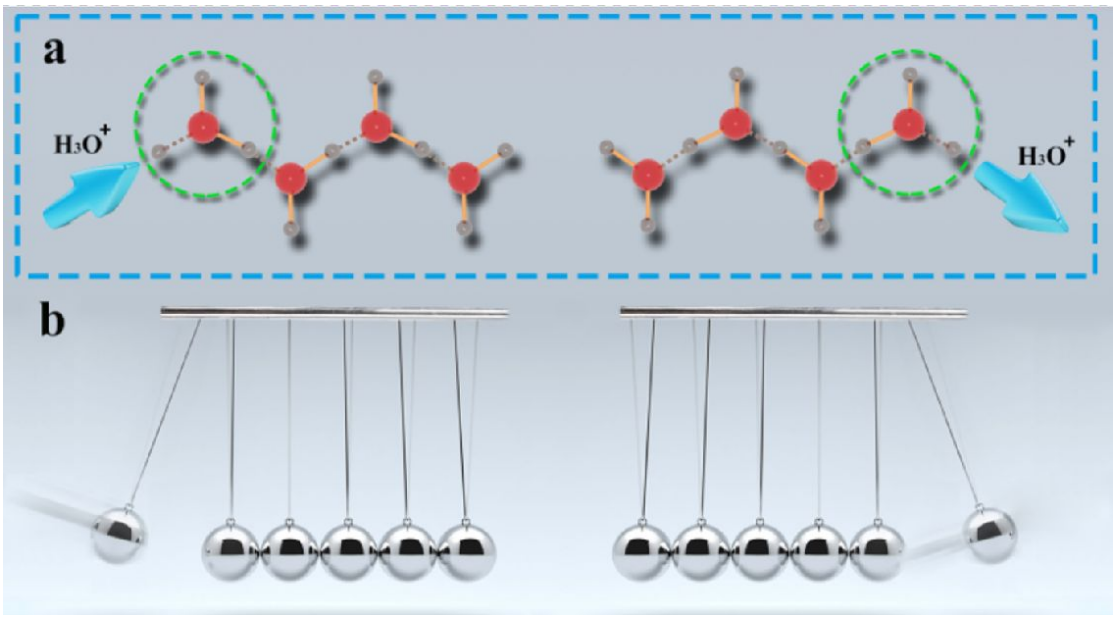

Figure S11. (a) An illustration of Grotthuss conduction. (b) An illustration for Newton's Cradle balance balls.

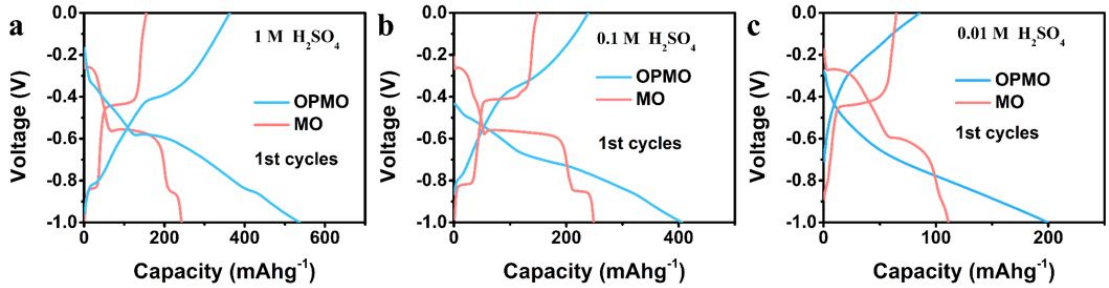

Figure S12. Galvanostatic charge/discharge (GCD) measurements for the first cycle in (a) 1 M, (b) 0.1 M, and (c) 0.01 M H_2SO_4 electrolyte.

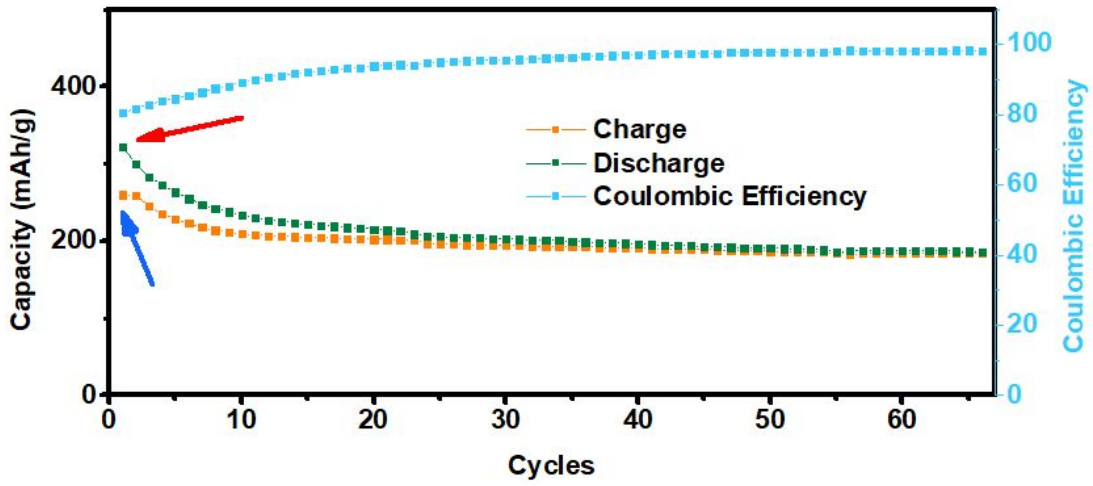

Figure S13. Cycling performance of OPMO at a current density of 0.5 A g^{-1}.

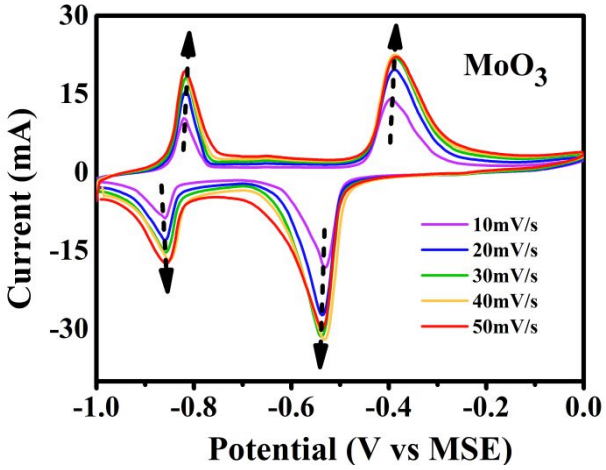

Figure S14. The CV curves of different scan rates.

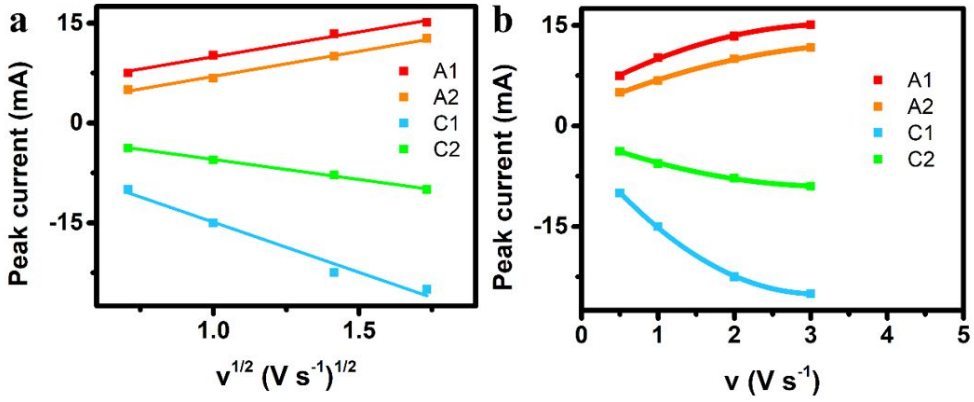

Figure S 15. (a) The plots of peak currents with the square root of scan rates. (b) The plots of peak currents with the scan rates. A1, A2, C1, C2 correspond to the CV peaks in Figure S16a.

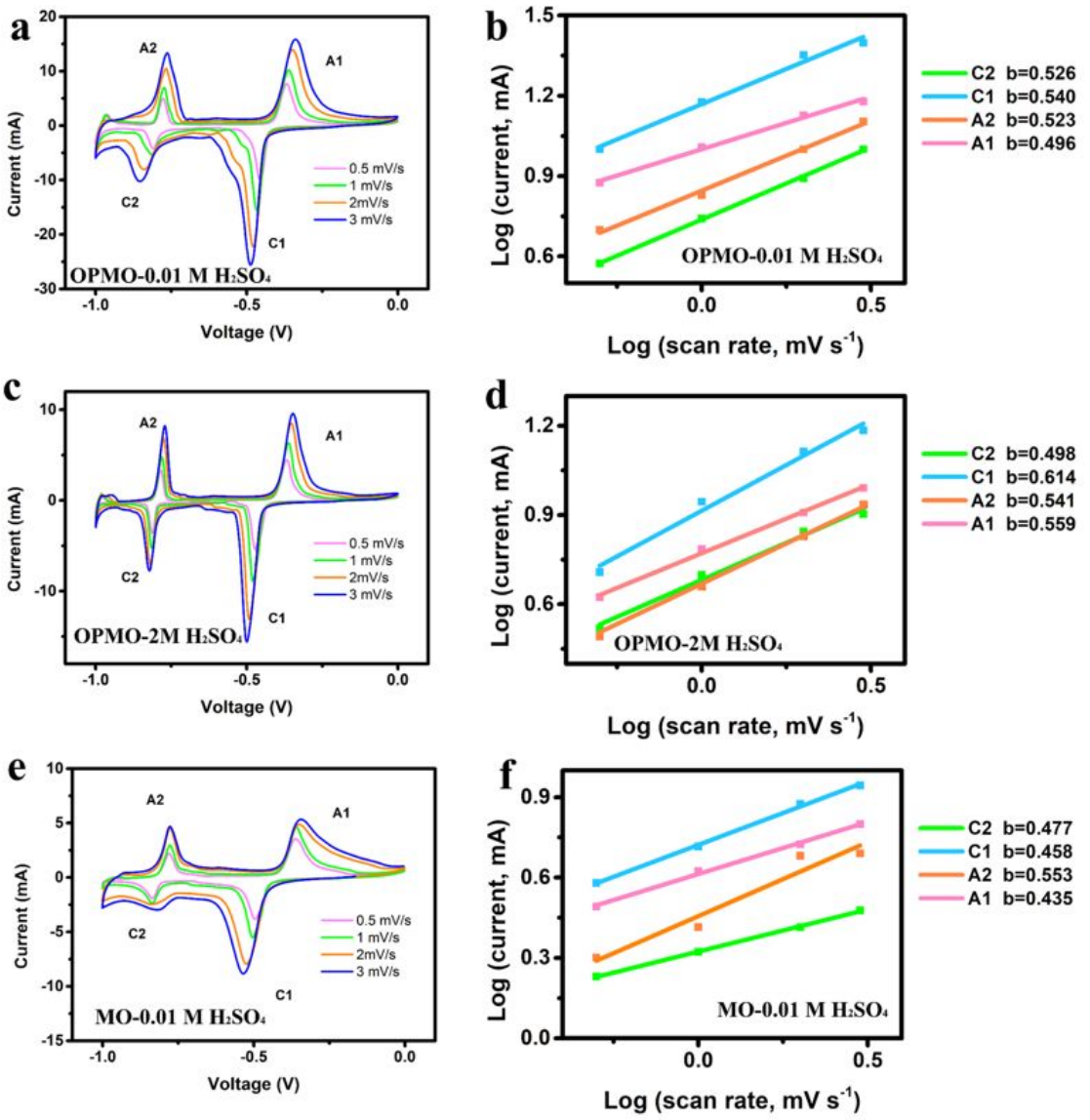

Figure S16. (a) Cyclic voltammetry (CV) of OPMO at various scan rates in 0.01 M H_2SO_4. (b) Log values of peak currents versus scan rates of (a). (c) Cyclic voltammetry (CV) of OPMO at various scan rates in 2 M H_2SO_4. (d) Log values of peak currents versus scan rates of (c). (e) Cyclic voltammetry (CV) of MO at various scan rates in 0.01 M H_2SO_4. (f) Log values of peak currents versus scan rates of (e).

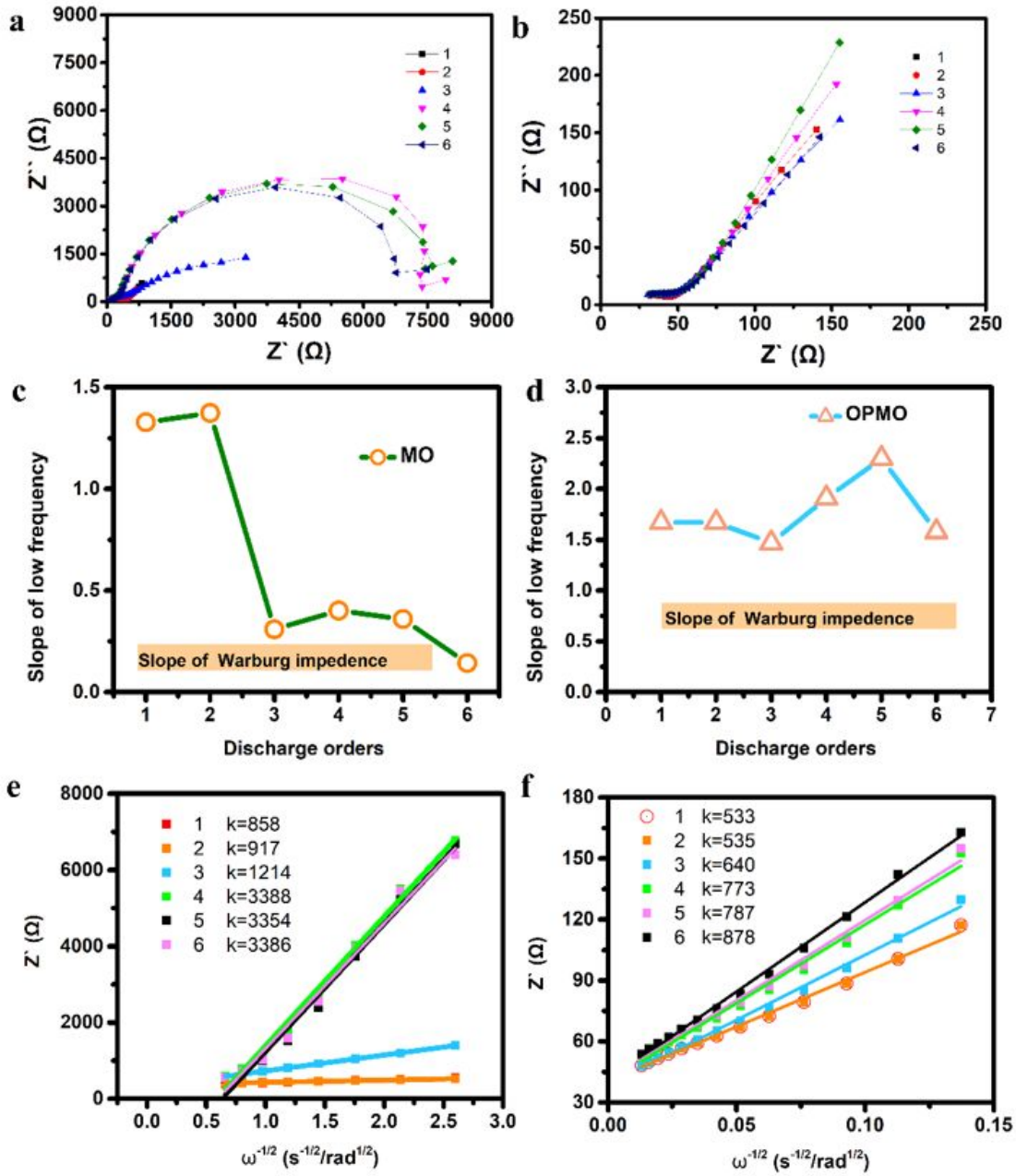

Figure S17. 2D curves of in situ EIS for OPMO and MO. (a) In-situ EIS 2D plot of MO. (b) In-situ EIS 2D plot of OPMO. (c) The slope of Warburg impedance for MO. (d) The slope of Warburg impedance for OPMO. (e) Bode plot for MO. (f) Bode plot for OPMO.

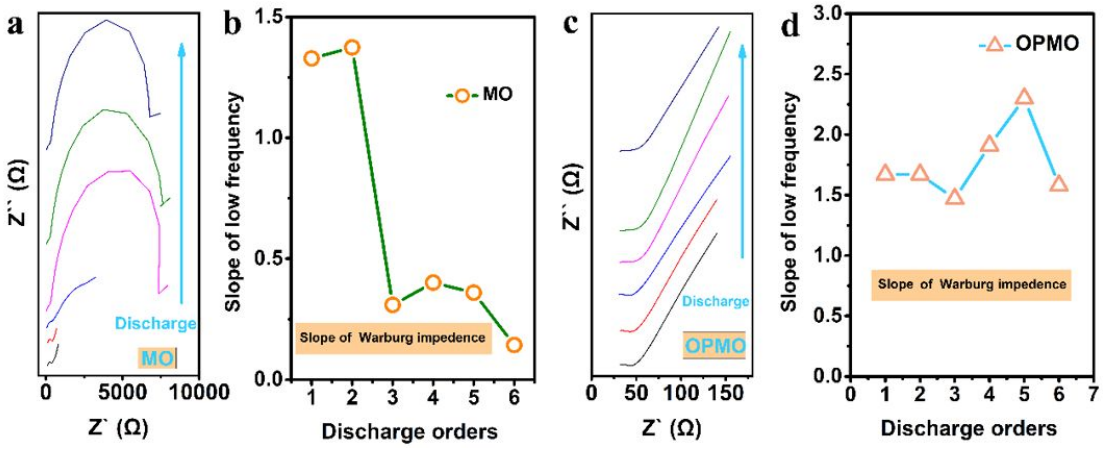

Figure S18. 2D curves of EIS for OPMO and MO. (a) In-situ EIS 2D plot of MO. (b) The slope of Warburg impedance for MO. (c) In-situ EIS 2D plot of OPMO. (d) The slope of Warburg impedance for OPMO.

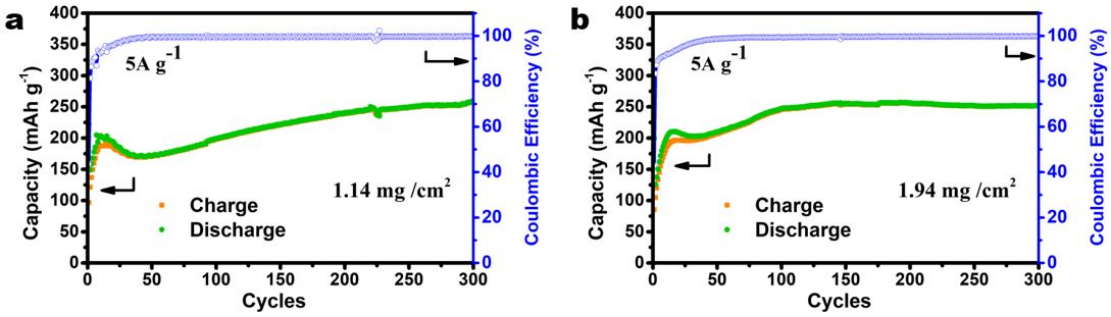

Figure S19. (a) Electrochemical performance of low mass loading of OPMO. (b) Electrochemical performance of low mass loading of OPMO.

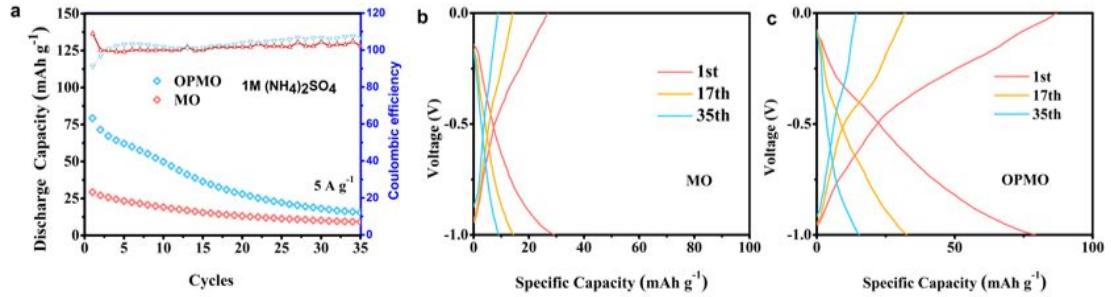

Figure S20. (a) The cycling performance of MO and OPMO in 1M $(NH_4)_2SO_4$. (b) GCD curves of MO for 1, 17, and 35 cycles. (c) GCD curves of OPMO for 1, 17, and 35 cycles.

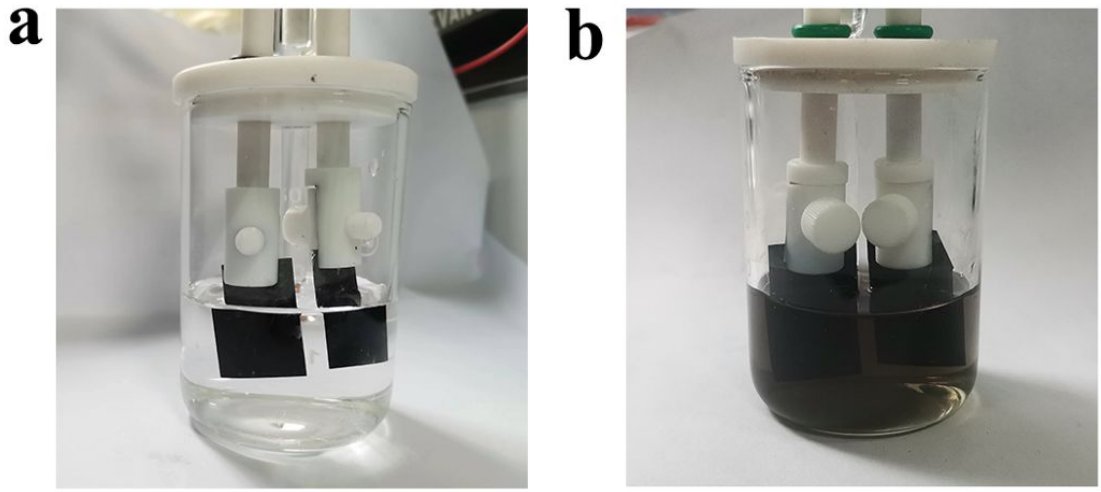

Figure S21. (a) OPMO electrode in 0.01 M H_2SO_4 after 10 cycles. (b) The OPMO electrode in 8 M H_2SO_4 after 10 cycles. OPMO electrode shows dramatic dissolving in strong acid.

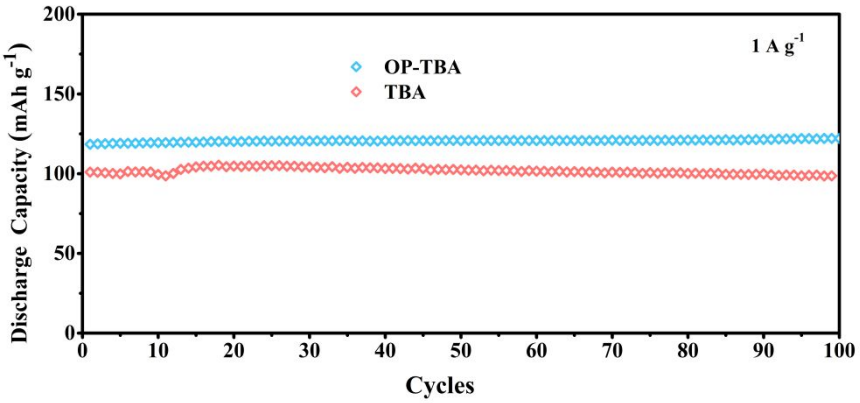

Figure S22. Electrochemical performance for TBA and OP-TBA (oxygen plasma treated TBA).

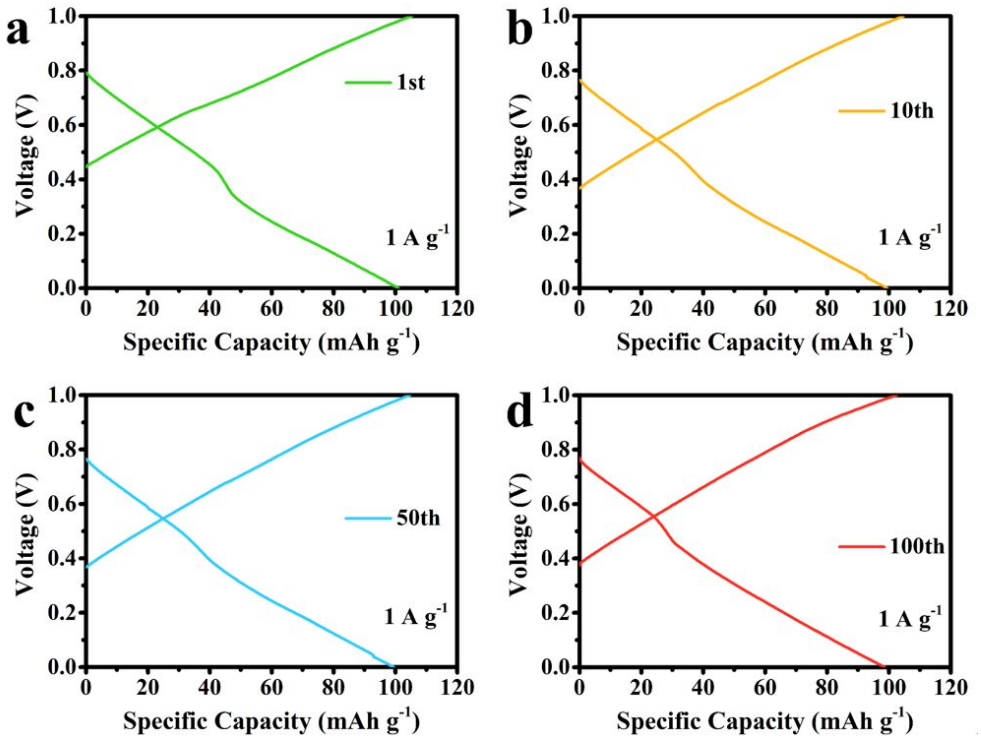

Figure S23. (a) Voltage-capacity curves for TBA cathode at 1st cycle in 0.01 M H_2SO_4. (b) Voltage-capacity curves for TBA cathode at 10th cycles in 0.01 M H_2SO_4. (c) Voltage-capacity curves for TBA cathode at 50th cycle in 0.01 M H_2SO_4. (d) Voltage-capacity curves for TBA cathode at 100th cycle in 0.01 M H_2SO_4.

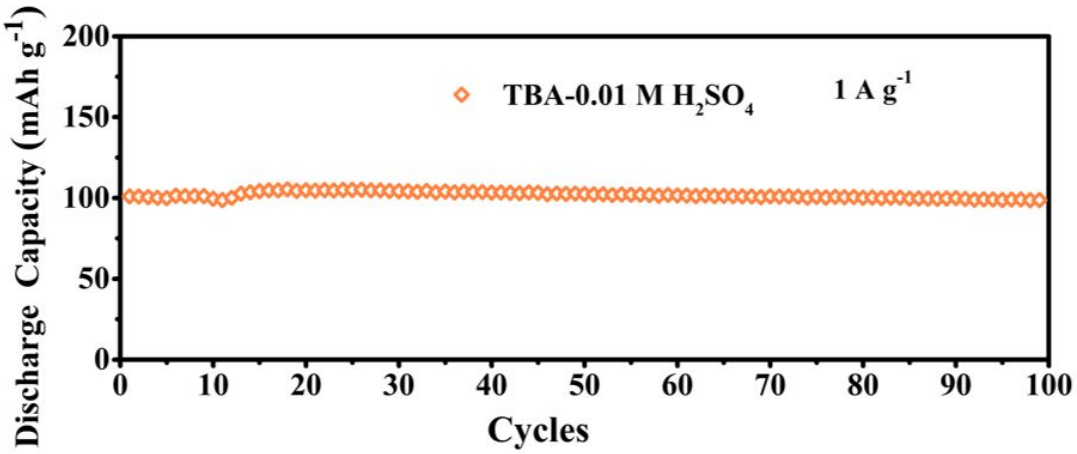

Figure S24. The cycling performance of TBA cathode in 0.01 M H_2SO_4 at 1 A g^{-1}.

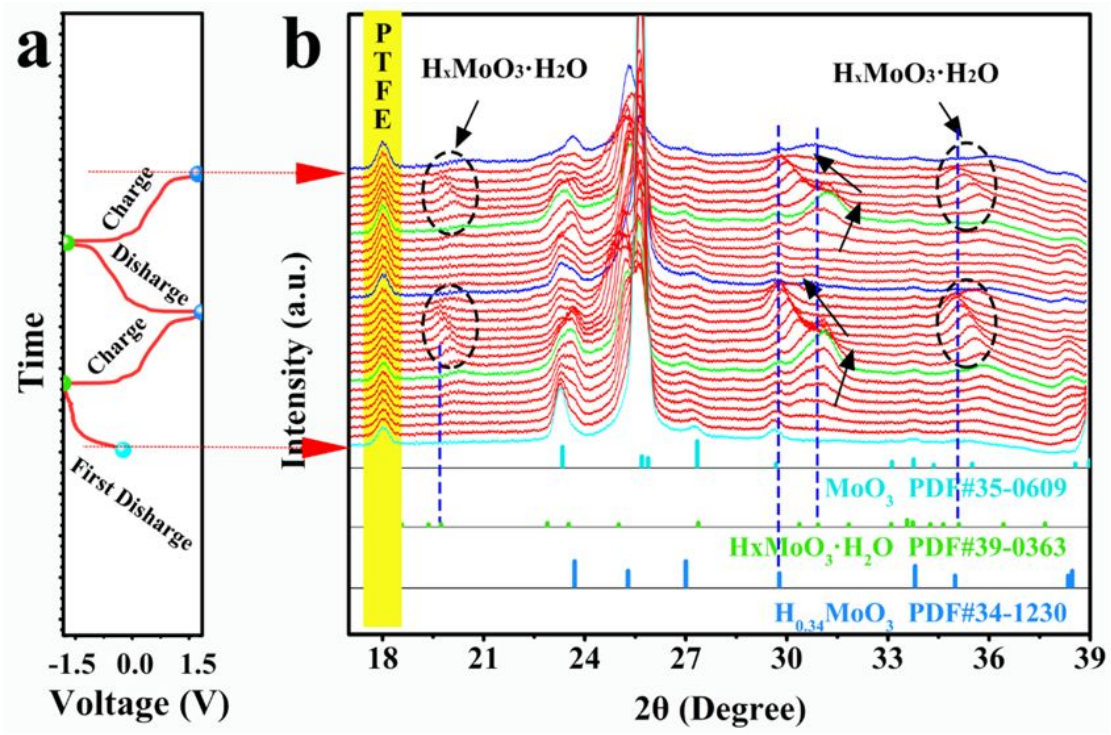

Figure S25. (a) Discharge/charge curves of OPMO. (b) In-situ XRD 1D pattern of OPMO electrode.

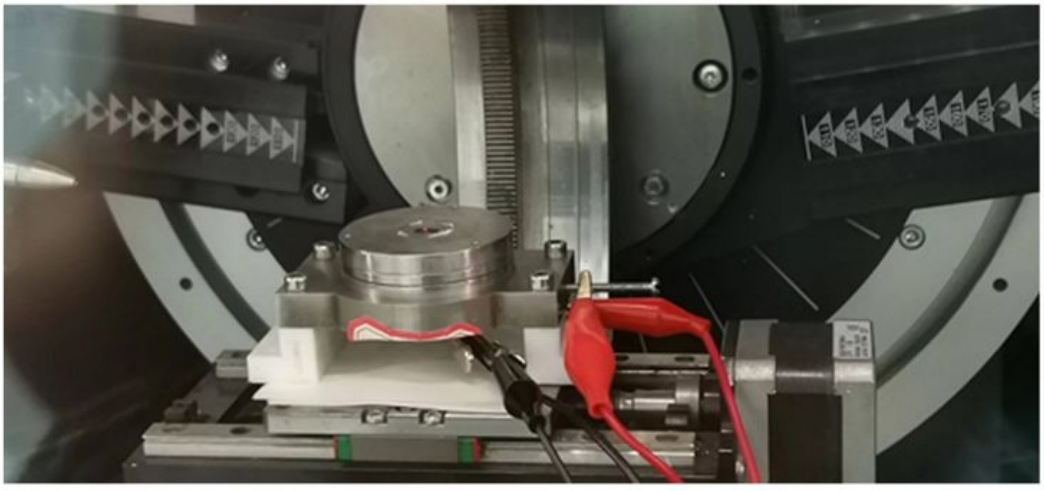

Figure S26. Schematic illustration for in situ XRD cell.

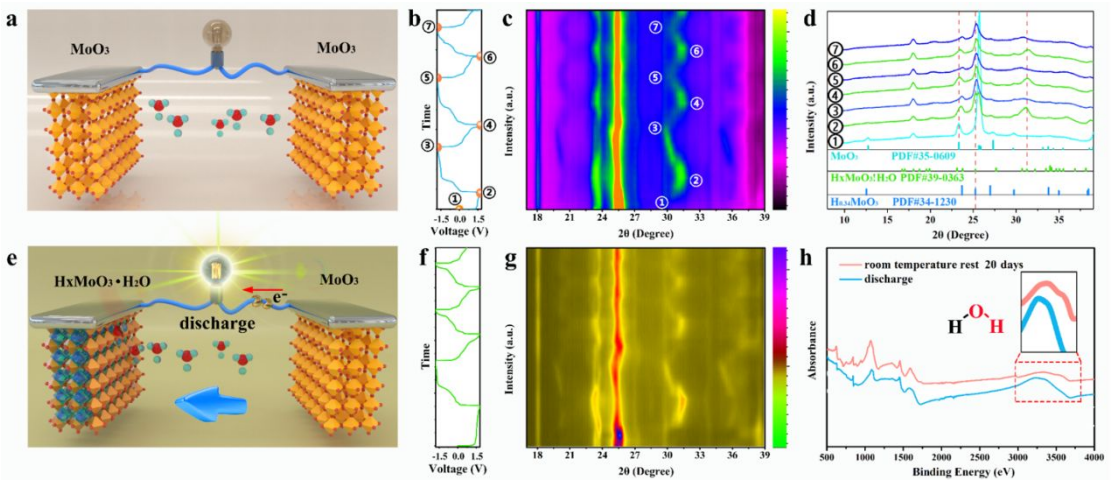

Figure S27. (a, e) Schematic illustration for symmetric cell with pristine and discharge. (b, f) Discharge/charge curves of OPMO sample at -1.8~1.8 V. (c, g) In-situ XRD 2D pattern of OPMO. (d) XRD patterns of full discharge and full charge states of OPMO. (h) FTIR plots of OPMO electrode after discharging at room temperature for 20 days.

First discharge: $MoO_3 + H_xH_2O^{x+} + x\ e^- \rightarrow H_xMoO_3 \cdot H_2O$

Charge: $H_xMoO_3 \cdot H_2O \leftrightarrow H_{0.34}MoO_3 + H_{(x-0.34)}H_2O^{(x-0.34)+} + (x-0.34)\ e^-$

Discharge: $H_{0.34}MoO_3 + H_{(x-0.34)}H_2O^{(x-0.34)+} + (x-0.34)\ e^- \leftrightarrow H_xMoO_3 \cdot H_2O$

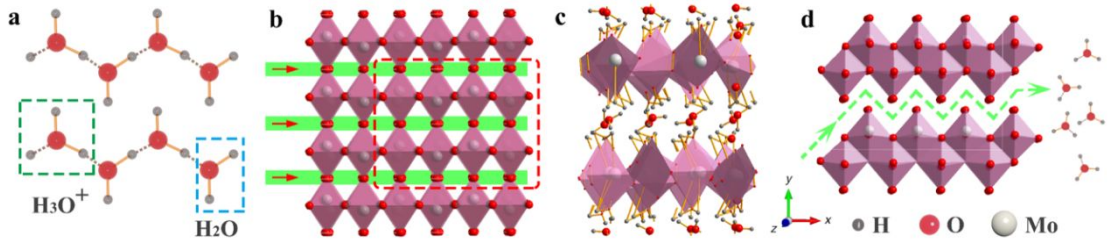

Figure S28. (a) Illustration for protons and hydroniums positions in proton electrolyte. (b) Initial MoO_3 crystal structure before the charge. (c) Full discharge crystal structure of $H_xMoO_3 \cdot H_2O$. (d) Full charge crystal structure of $H_{0.34}MoO_3$.

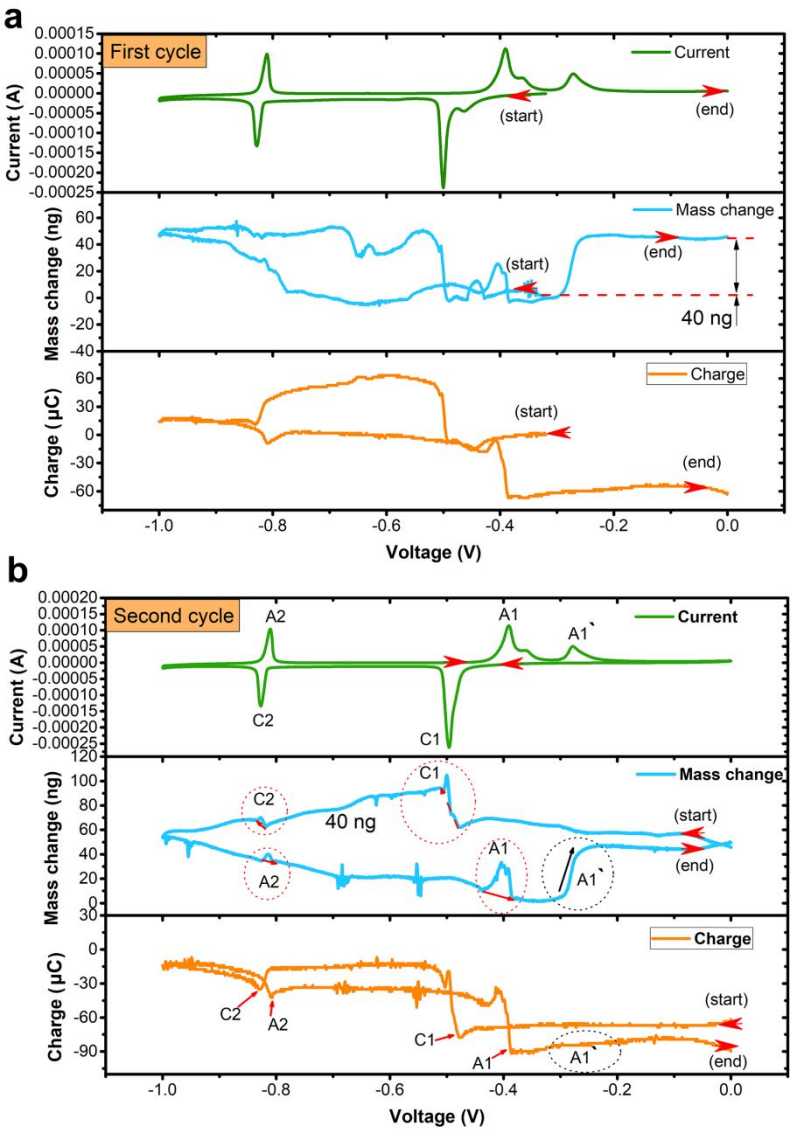

Figure S29. (a) The first cycle of CV result and QCM results for OPMO at a scan rate of 10 mV s^{-1} and corresponding mass changes and charge variations. (b) The second cycle of CV result and QCM results for OPMO at a scan rate of 10 mV s^{-1} and corresponding mass changes and charge variations.

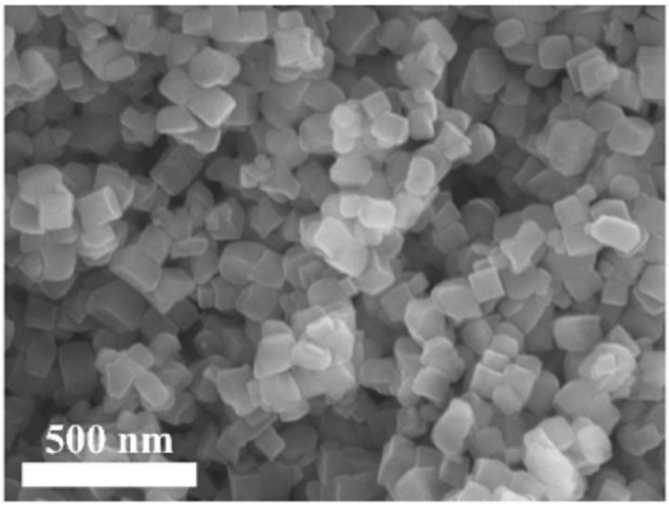

Figure S30. SEM image of CuFe-TBA material.

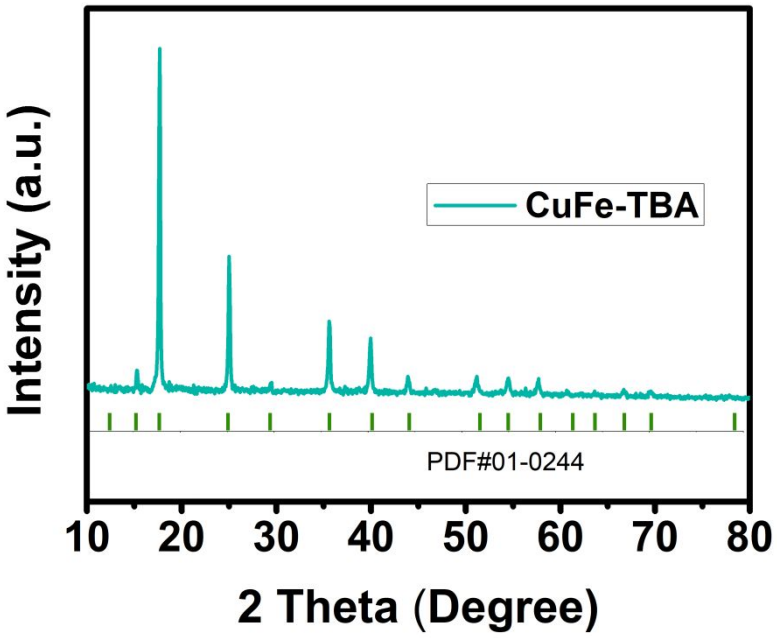

Figure S31. XRD pattern of CuFe-TBA material.

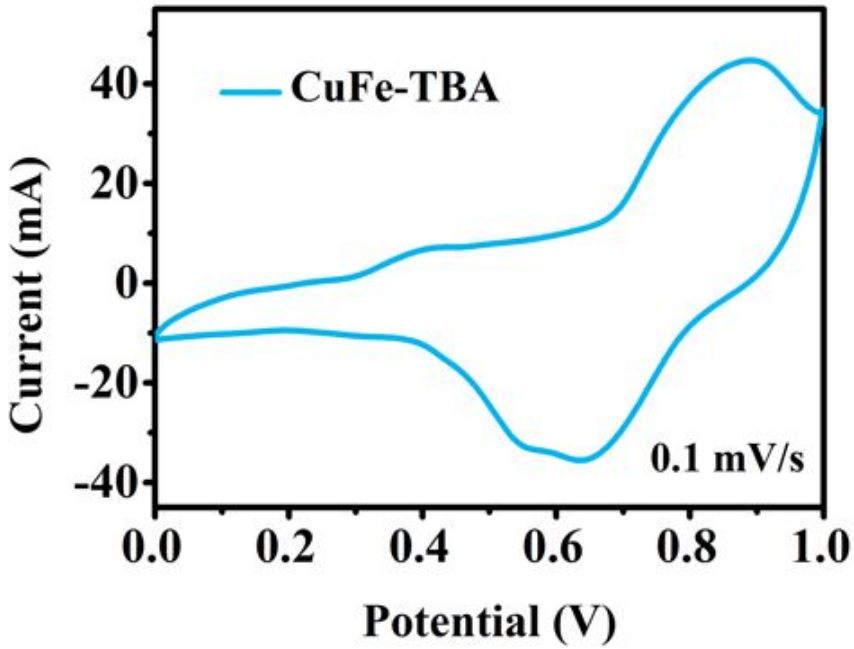

Figure S32. TBA electrode CV curve in 0.01 M H_2SO_4 electrolyte with three-electrode in 0.1 mV/s, TBA electrode is the working electrode, carbon cloth is a counter electrode, and SCE is the reference electrode.

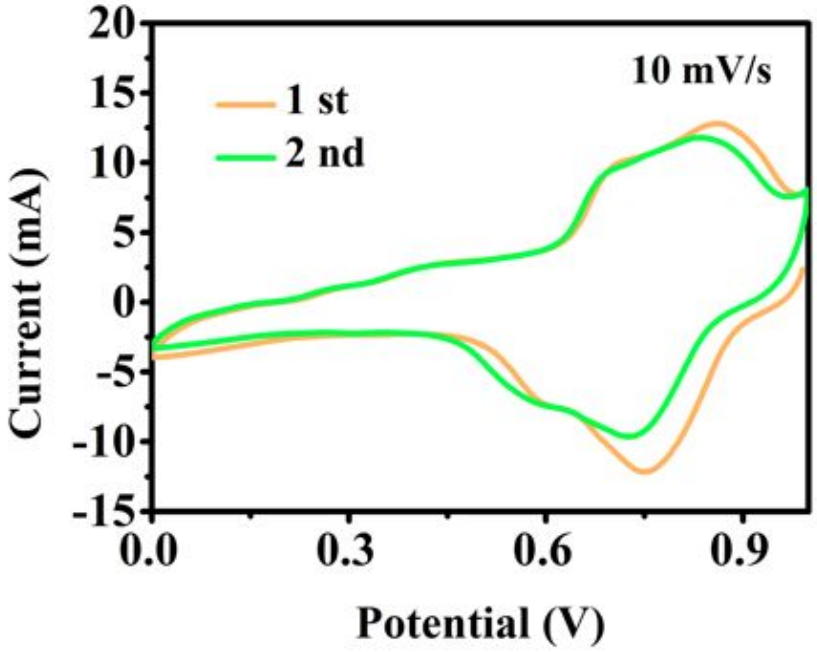

Figure S33. CV curve of OPMO//CuFe-TBA full battery.

Figure S34. Open the current potential of OPMO//CuFe-TBA full battery after the first charge.

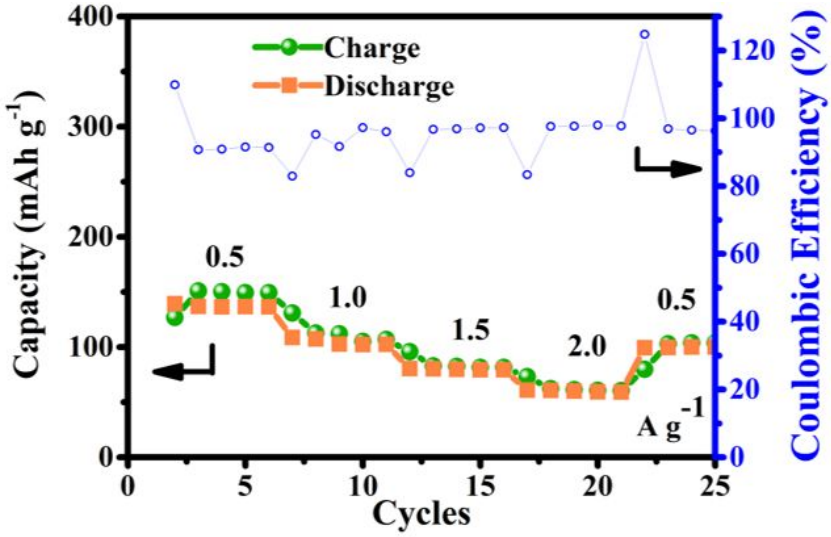

Figure S35. Electrochemical performances of the full cell, the electrochemical test starts at rates of 0.5, 1.0, 1.5, and 2.0 A g^{-1}.

Figure S36. Full cell application in LED device.

Figure S37. Full cell application in LCD (liquid crystal display).

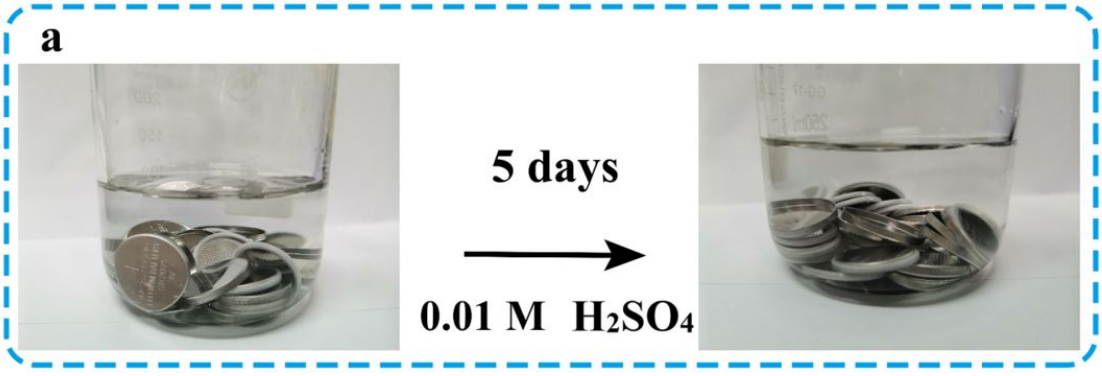

Figure S38. The coin cell shells in 0.01 M H_2SO_4 for 5 days.

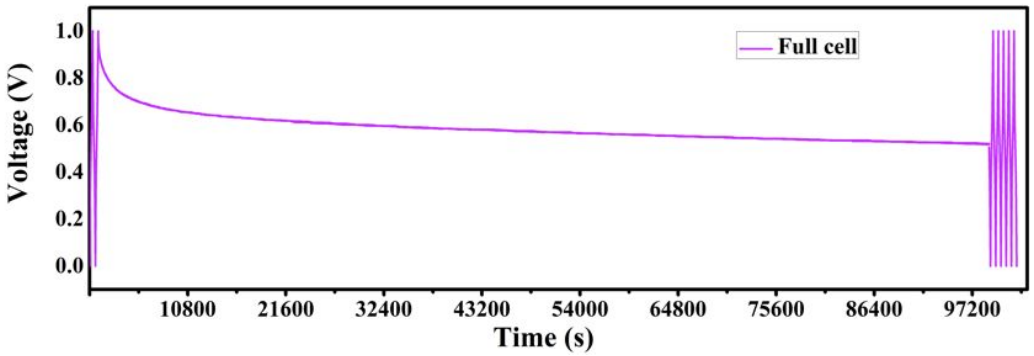

Figure S39. Voltage-time plot for proton full cell after long-time of resting.

Table S1. pH and conductivity value for different electrolytes.

Acid electrolyte	5 M H_2SO_4	1 M H_2SO_4	0.1 M H_2SO_4	0.01 M H_2SO_4
pH	0.51	0.13	0.83	1.51
Conductivity (**mS cm^{-1}**)	553	340	52.1	5.49
Water electrolyte	Tap water	RO water	UP water	Distilled water
pH	6.88	7.15	7.35	7.50
Conductivity (**μS cm^{-1}**)	313	158	3.76	4.23
The ionic concentration of Na (mg L^{-1})	6.5871	0.1944	0.006	0.009

Table S2 Inorganic electrode materials and battery factors for APBs

Three-electrode cell (TEC), Swagelok cells (SC), Coin cell (CC), Pouch cell (PC)

Cell composition				Ref.
Cathode	Anode	Electrolyte	Cell type	
CuTBA	**α-MoO_3**	**0.01 M H_2SO_4**	TEC	**This**

$(Cu(Fe(CN)_6)_3 \cdot 3.4H_2O)$		**DI water**	SC CC PC	**work**
$Cu(Fe(CN)_6)_3 \cdot 3.4H_2O$	**Activated carbon**	1M H_3PO_4/MeCN	TEC SC	[1]
CuHCF	**H_2 anode**	5M H_3PO_4	SC	[2]
$Ni(Fe(CN)_6)_3 \cdot 4H_2O$	**Carbon film**	1.0 M H_2SO_4	TEC CC	[3]
$V(Fe(CN)_6)_3 \cdot 4H_2O$	**Graphite plate**	6.0 M H_2SO_4	TEC	[4]
$Cu(Fe(CN)_6)_1 \cdot 3.4H_2O$	**Activated carbon**	2.0 M H_2SO_4	TEC	[5]
$Cu(Fe(CN)_6)_{2/3} \cdot 4H_2O$	**MoO_3**	2.0 M H_2SO_4	TEC	[6]
MnO_2	**MoO_3**	2.0 M H_2SO_4 + 2.0 M $MnSO_4$).	TEC	[7]
Carbon paper	**MoO_3**	1.0 M H_2SO_4	TEC	[8]
$Cu(Fe(CN)_6)_3 \cdot 4H_2O$	**α-MoO_3**	9.5 M H_3PO_4	TEC	[9]
Graphite	**α-MoO_3**	6.0 M H_2SO_4	TEC	[10]
Graphite	**α-MoO_3**	4.4 M H_2SO_4	TEC	[11]
Carbon fiber paper	**α-MoO_3**	5.0M glucose + 4.2 M H_2SO_4	TEC	[12]

Carbon rod	**MoO_3@TiO_2**	1.0 M H_2SO_4 + 1.0 M $MnSO_4$	TEC	[13]
Over capacitive carbon	**H_xIrO_4**	0.5 M $HClO_4$	SC	[14]
Pt film	**V_2O_5**	0.4M CF_3COOH	TEC	[15]
Pt electrodes	**TiO_2**	1.0 M acetate	TEC	[16]
Graphite electrode	**TiO_2**	0.5 M H_2SO_4 + 2.0 M $MnSO_4$	TEC	[17]
Platinum wire	**$H_2Ti_3O_7$**	3.0 M H_2SO_4	TEC	[18]
Activated carbon	**$WO_3 \cdot 0.6H_2O$**	0.1 M H_2SO_4 + 3.0 M HCl	TEC CC	[19]
rGO (Reduced graphene oxide)	**Ti_3C_2Tx**	1.0 M H_2SO_4	TEC	[20]
AC (Activated carbon)	**Ti_3C_2Tx** (MXene)	3.0 M H_2SO_4	TEC SC.	[21]

Table S3 Organic electrodes and battery factors for APBs.

Cell composition				Ref.
Cathode	Anode	Electrolyte	Cell type	
TCHQ- ZTC (Tetrachlorohydroquinone	**AQ** (anthraquinone-Zeolite	0.5 M H_2SO_4	TEC	[22]

-Zeolite templated carbon)	templated carbon)			
DDAQ (Alizarin)	**DDAQ** (Alizarin)	1.0 M H_2SO_4	TEC	[23]
PEDOT-BQH (poly(3,4-ethylenedioxythiophene-benzoquinone)	**PEDOT-AQ** (poly-3,4-ethylene dioxythiophene-anthraquinone)	0.1 M pyridine in MeCN	TEC	[24]
pEP(QH$_2$)E (poly-ethylene dioxythiophene-propylenedioxythiophene-hydroquinone)	**pEP(NQ)E** (poly-ethylene dioxythiophene-propylenedioxythiophene- naphthoquinone)	0.5 M H_2SO_4	CC	[25]
TCHQ (Tetrachlorohydroquinone)	**AQ** (anthraquinone)	0.5 M H_2SO_4	TEC	[22]
BQ (benzoquinone)	**Pt**	0.5 M H_2SO_4	TEC	[26]
Tiron-CC (4,5Dihydroxy-1,3-benzenedisulfonate-adsorbed carbon cloth)	**AQDS** (2,7-anthraquinone disulfonate)	1.0 M H_2SO_4	TEC	[27]

BQhMdA-CNT (benzoquinone-alt-hexamethyl Lene diamine)	**Platinum wire**	0.1 M $HClO_4$	SC	[28]
BQpPhdA-CNT (benzoquinone-alt-pphenylenediamine)	**Platinum wire**	0.1 M $HClO_4$	SC	[28]
QZ-EPE (quinizarin-ethynylpentiptycenylethynylene)	**NQ-EPE** (Naphthoquinone-ethynylpentiptycenylethynylene)	0.1 M MeTriHTFSI /MeCN/H_2O	TEC	[29]
AC (Activated carbon)	**PTCDA** (3,4,9,10perylenetetracarboxylic dianhydride)	1.0 M H_2SO_4	TEC	[30]
$\mathbf{H_{1.1}K_{0.2}In_{0.9}Fe(CN)_6}$	**DPPZ** (dipyridophenazine)	0.5 M H_2SO_4	TEC	[31]
pDTP-NQ (poly dithieno 3,2-b:2',3'-d pyrrole-naphthoquinone)	**pDTP-AQ** (poly dithieno 3,2-b:2',3'-d pyrrole-anthraquinone)	1.0 M H_2SO_4	CC	[32]
Carbon felt	**ALO**	2.0 M HBF_4 +	TEC	[33]

	(Alloxazine)	2.0 M $Mn(BF_4)_2$		
MnO_2@GF (graphite felt)	**PTO** (pyrene-4,5,9,10-tetraone)	2.0 M $MnSO_4$ +2.0 M H_2SO_4	TEC Pouch cell	[34]

Note: The electrolyte solution is an aqueous solution if not mentioned specifically.

References

1. Xu, Y.; Wu, X.; Jiang, H.; Tang, L.; Koga, K. Y.; Fang, C.; Lu, J.; Ji, X., A non-aqueous H_3Po_4 electrolyte enables stable cycling of proton electrodes. *Angew. Chem. Int. Ed.* **2020,** *59* (49), 22007-22011.

2. Zhu, Z.; Wang, W.; Yin, Y.; Meng, Y.; Liu, Z.; Jiang, T.; Peng, Q.; Sun, J.; Chen, W., An ultrafast and ultra-low-temperature hydrogen gas-proton battery. *J. Am. Chem. Soc.* **2021,** *143* (48), 20302-20308.

3. Wu, X.; Qiu, S.; Xu, Y.; Ma, L.; Bi, X.; Yuan, Y.; Wu, T.; Shahbazian-Yassar, R.; Lu, J.; Ji, X., Hydrous nickel–iron Turnbull's blue as a high-rate and low-temperature proton electrode. *ACS Appl. Mater. Interfaces* **2020,** *12* (8), 9201-9208.

4. Peng, X.; Guo, H.; Ren, W.; Su, Z.; Zhao, C., Vanadium hexacyanoferrate as high-capacity cathode for fast proton storage. *Chem. Commun.* **2020,** *56* (79), 11803-11806.

5. Wu, X.; Hong, J. J.; Shin, W.; Ma, L.; Liu, T.; Bi, X.; Yuan, Y.; Qi, Y.; Surta, T. W.; Huang, W.; Neuefeind, J.; Wu, T.; Greaney, P. A.; Lu, J.; Ji, X., Diffusion-free Grotthuss topochemistry for high-rate and long-life proton batteries. *Nat. Energy* **2019,** *4* (2), 123-130.

6. Ma, N.; Kosasang, S.; Yoshida, A.; Horike, S., Proton-conductive coordination polymer glass for solid-state anhydrous proton batteries. *Chem. Sci.* **2021**, 5818–5824.

7. Yan, L.; Huang, J.; Guo, Z.; Dong, X.; Wang, Z.; Wang, Y., Solid-state proton battery operated at ultralow temperature. *ACS Energy Lett.* **2020,** *5* (2), 685-691.

8. Wang, X.; Xie, Y.; Tang, K.; Wang, C.; Yan, C., Redox chemistry of molybdenum trioxide for ultrafast hydrogen-ion storage. *Angew. Chem. Int. Ed.* **2018,** *57* (36), 11569-11573.

9. Jiang, H.; Shin, W.; Ma, L.; Hong, J. J.; Wei, Z.; Liu, Y.; Zhang, S.; Wu, X.; Xu, Y.; Guo, Q.; Subramanian, M. A.; Stickle, W. F.; Wu, T.; Lu, J.; Ji, X., A high-rate aqueous proton battery delivering power below −78 °c via an unfrozen phosphoric acid. *Adv. Energy Mater.* **2020,** *10* (28), 2000968.

10. Su, Z.; Ren, W.; Guo, H.; Peng, X.; Chen, X.; Zhao, C., Ultrahigh areal capacity hydrogen-ion batteries with MoO_3 loading over 90 mg cm^{-2}. *Adv. Funct. Mater.* **2020,** *30* (46), 2005477.

11. Guo, H.; Goonetilleke, D.; Sharma, N.; Ren, W.; Su, Z.; Rawal, A.; Zhao, C., Two-Phase Electrochemical Proton Transport and Storage in α-MoO3 for Proton Batteries. *Cell Reports Physical Science* **2020,** *1* (10), 100225.

12. Su, Z.; Chen, J.; Ren, W.; Guo, H.; Jia, C.; Yin, S.; Ho, J.; Zhao, C., "Water-in-sugar" electrolytes enable ultrafast and stable electrochemical naked proton storage. *Small* **2021,** *17* (40), e2102375.

13. Wang, C.; Zhao, S.; Song, X.; Wang, N.; Peng, H.; Su, J.; Zeng, S.; Xu, X.; Yang,

J., Suppressed Dissolution and Enhanced Desolvation in Core–Shell MoO_3 @TiO_2 Nanorods as a High-Rate and Long-Life Anode Material for Proton Batteries. *Adv. Energy Mater.* **2022,** *12* (19).

14. Lemaire, P.; Sel, O.; Alves Dalla Corte, D.; Iadecola, A.; Perrot, H.; Tarascon, J. M., Elucidating the origin of the electrochemical capacity in a proton-based battery H_xIrO_4 via advanced electrogravimetry. *ACS Appl. Mater. Interfaces* **2020,** *12* (4), 4510-4519.

15. Buchheit, A.; Tessmer, B.; Munoz-Castro, M.; Bracht, H.; Wiemhofer, H. D., Electrochemical proton intercalation in vanadium pentoxide thin films and its electrochromic behavior in the near-ir region. *ChemistryOpen* **2021,** *10* (3), 340-346.

16. Kim, Y. S.; Harris, K. D.; Limoges, B.; Balland, V., On the unsuspected role of multivalent metal ions on the charge storage of a metal oxide electrode in mild aqueous electrolytes. *Chem Sci* **2019,** *10* (38), 8752-8763.

17. Geng, C.; Sun, T.; Wang, Z.; Wu, J. M.; Gu, Y. J.; Kobayashi, H.; Yang, P.; Hai, J.; Wen, W., Surface-induced desolvation of hydronium ion enables anatase tio2 as an efficient anode for proton batteries. *Nano Lett.* **2021,** *21* (16), 7021-7029.

18. Fleischmann, S.; Sun, Y.; Osti, N. C.; Wang, R.; Mamontov, E.; Jiang, D.-e.; Augustyn, V., Interlayer separation in hydrogen titanates enables electrochemical proton intercalation. *J. Mater. Chem. A* **2020,** *8* (1), 412-421.

19. Jiang, H.; Hong, J. J.; Wu, X.; Surta, T. W.; Qi, Y.; Dong, S.; Li, Z.; Leonard, D. P.; Holoubek, J. J.; Wong, J. C.; Razink, J. J.; Zhang, X.; Ji, X., Insights on the proton

insertion mechanism in the electrode of hexagonal tungsten oxide hydrate. *J. Am. Chem. Soc.* **2018,** *140* (37), 11556-11559.

20. Wang, S.; Zhao, X.; Yan, X.; Xiao, Z.; Liu, C.; Zhang, Y.; Yang, X., Regulating fast anionic redox for high-voltage aqueous hydrogen-ion-based energy storage. *Angew. Chem. Int. Ed.* **2019,** *58* (1), 205-210.

21. Lukatskaya, M. R.; Kota, S.; Lin, Z. F.; Zhao, M. Q.; Shpigel, N.; Levi, M. D.; Halim, J.; Taberna, P. L.; Barsoum, M.; Simon, P.; Gogotsi, Y., Ultra-high-rate pseudocapacitive energy storage in two-dimensional transition metal carbides. *Nat. Energy* **2017,** *2* (8), 1-6.

22. Tomai, T.; Mitani, S.; Komatsu, D.; Kawaguchi, Y.; Honma, I., Metal-free aqueous redox capacitor via proton rocking-chair system in an organic-based couple. *Scientific Reports* **2014,** *4*, 3591.

23. Tong, L.; Jing, Y.; Gordon, R. G.; Aziz, M. J., Symmetric all-quinone aqueous battery. *ACS Appl. Energy Mater.* **2019,** *2* (6), 4016-4021.

24. Emanuelsson, R.; Sterby, M.; Stromme, M.; Sjodin, M., An all-organic proton battery. *J. Am. Chem. Soc.* **2017,** *139* (13), 4828-4834.

25. Strietzel, C.; Sterby, M.; Huang, H.; Stromme, M.; Emanuelsson, R.; Sjodin, M., An aqueous conducting redox-polymer-based proton battery that can withstand rapid constant-voltage charging and sub-zero temperatures. *Angew. Chem. Int. Ed.* **2020,** *59* (24), 9631-9638.

26. Christudas Dargily, N.; Thimmappa, R.; Manzoor Bhat, Z.; Devendrachari, M. C.;

Kottaichamy, A. R.; Gautam, M.; Shafi, S. P.; Thotiyl, M. O., A rechargeable hydrogen battery. *J. Phys. Chem. Lett.* **2018,** *9* (10), 2492-2497.

27. Xu, Y.; Zheng, Y.; Wang, C.; Chen, Q., An all-organic aqueous battery powered by adsorbed quinone. *ACS Appl. Mater. Interfaces* **2019,** *11* (26), 23222-23228.

28. Navarro-Suárez, A. M.; Carretero-González, J.; Rojo, T.; Armand, M., Poly(quinone-amine)/nanocarbon composite electrodes with enhanced proton storage capacity. *J. Mater. Chem. A* **2017,** *5* (44), 23292-23298.

29. Wang, H.; Emanuelsson, R.; Karlsson, C.; Jannasch, P.; Stromme, M.; Sjodin, M., Rocking-chair proton batteries with conducting redox polymer active materials and protic ionic liquid electrolytes. *ACS Appl. Mater. Interfaces* **2021,** *13* (16), 19099-19108.

30. Wang, X.; Bommier, C.; Jian, Z.; Li, Z.; Chandrabose, R. S.; Rodriguez-Perez, I. A.; Greaney, P. A.; Ji, X., Hydronium-ion batteries with perylenetetracarboxylic dianhydride crystals as an electrode. *Angew. Chem. Int. Ed.* **2017,** *56* (11), 2909-2913.

31. Qiao, J.; Qin, M.; Shen, Y. M.; Cao, J.; Chen, Z.; Xu, J., A rechargeable aqueous proton battery based on a dipyridophenazine anode and an indium hexacyanoferrate cathode. *Chem. Commun.* **2021,** *57* (35), 4307-4310.

32. Wang, X.; Zhou, J.; Tang, W., Poly(dithieno[3,2-b:2’,3’-d]pyrrole) twisting redox pendants enabling high current durability in all-organic proton battery. *Energy Storage Mater.* **2021,** *36*, 1-9.

33. Sun, T.; Du, H.; Zheng, S.; Shi, J.; Tao, Z., High power and energy density aqueous

proton battery operated at −90 ° C. *Adv. Funct. Mater.* **2021**, 2010127.

34. Guo, Z.; Huang, J.; Dong, X.; Xia, Y.; Yan, L.; Wang, Z.; Wang, Y., An organic/inorganic electrode-based hydronium-ion battery. *Nat. Commun.* **2020,** *11* (1), 959.